Articles

Backbone Dynamics of *Fusarium solani pisi* Cutinase Probed by Nuclear Magnetic Resonance: The Lack of Interfacial Activation Revisited†

Jeanine J. Prompers,‡ Anneke Groenewegen,§ Cornelis W. Hilbers,‡ and Henri A. M. Pepermans*,§

NSR Center for Molecular Structure, Design and Synthesis, Laboratory of Biophysical Chemistry, University of Nijmegen, Toernooiveld, 6525 ED Nijmegen, The Netherlands, and Unilever Research, Olivier van Noortlaan 120, 3133 AT Vlaardingen, The Netherlands

Received November 16, 1998; Revised Manuscript Received February 22, 1999

ABSTRACT: The backbone dynamics of *Fusarium solani pisi* cutinase has been studied by a variety of nuclear magnetic resonance experiments to probe internal motions on different time scales. The core of cutinase appears to be highly rigid. The binding site, including the oxyanion hole, is mobile on the microsecond to millisecond time scale, in contrast to the well-defined active site and preformed oxyanion hole elucidated by X-ray crystallography [Martinez, C., de Geus, P., Lauwereys, M., Matthyssens, G., and Cambillau, C. (1992) *Nature 356,* 615−618]. In this crystal structure, cutinase has a rather open conformation, in which the hydrophobic binding site is exposed. The observed mobility in solution most likely represents the interconversion between open and more closed conformations, like in a true lipase. The opening and closing motions are on a time scale which corresponds with the kinetics of the hydrolysis reaction, i.e., the millisecond range, which suggests that these conformational rearrangements form the rate-limiting step in catalysis. We conclude that the crystal structure probably represents one of the multiple conformations present in solution, which fortuitously is the active conformation. The implications of our findings are discussed with particular reference to the explanation of the lack of interfacial activation as found for cutinase.

Proteins in solution undergo a wide variety of motions, ranging from atomic fluctuations and bond oscillations to hinge-bending motions, helix−coil transitions, and local and global unfolding processes (*1*−*3*). Detailed knowledge of protein dynamics is essential to understanding protein function and stability. Nuclear magnetic resonance (NMR)[1] spectroscopy in particular has been able to provide experimental evidence for a wide range of dynamical events in proteins at the atomic level (*4*, *5*). Here we apply NMR to probe the internal backbone mobility of *Fusarium solani pisi* cutinase.

F. solani pisi cutinase belongs to a group of homologous enzymes capable of degrading cutin (*6*), the insoluble lipid−polyester matrix covering the surface of plants. Cutinases are produced by several phytopathogenic fungi and pollen, enabling them to gain entry into the plant by enzymatic digestion of its cuticle. In addition, these enzymes degrade both monomeric and aggregated triglycerides (*6*−*8*). In contrast to true lipases (*9*), however, *F. solani pisi* cutinase shows no enhancement of its activity in the presence of a lipid−water interface (*7*, *8*).

The crystal structure of *F. solani pisi* cutinase has been solved to 1.0 Å resolution (*10*, *11*). It is an α/β hydrolase fold enzyme (*12*), consisting of a central β-sheet of five parallel strands covered by four α-helices. The catalytic apparatus of cutinase is composed of the catalytic triad Ser^{120}, His^{188}, and Asp^{175} and an oxyanion hole (main chain nitrogens of Ser^{42} and Gln^{121} and the O^{γ} of Ser^{42}) (*13*).

In classical lipases in aqueous solution, the hydrophobic binding site is buried by a lid, which supposedly helps the enzyme to avoid aggregation. During adsorption to a lipid layer, a significant rearrangement of this lid increases the hydrophobic surface area at the lipid-binding region, improving adsorption and allowing binding of the substrate. At the same time, the oxyanion hole atoms move to their proper positions to facilitate the nucleophilic attack of the substrate by the active site serine through polarization of the carbonyl group of the ester (*14*−*16*). In contrast to classical lipases, *F. solani pisi* cutinase does not possess a pronounced lid

† J.J.P. was supported by a grant from Unilever Research (URV 10087).

* Corresponding author. Telephone: 31-10-4605508. Fax: 31-10-4605192. E-mail: Rik.Pepermans@Unilever.com.

‡ University of Nijmegen.

§ Unilever Research.

[1] Abbreviations: NMR, nuclear magnetic resonance; MD, molecular dynamics; water-NOESY, nuclear Overhauser enhancement spectroscopy; water-ROESY, rotating-frame Overhauser enhancement spectroscopy;
PHOGSY, protein hydration observed by gradient spectroscopy; NOE, nuclear Overhauser effect; ROE, rotating-frame Overhauser effect; HSQC, heteronuclear single-quantum coherence spectroscopy; TPPI, time-proportional phase incrementation; GARP, globally optimized alternating phase rectangular pulse; PFG, pulsed field gradient; CW, continuous wave.

10.1021/bi9827215 CCC: $18.00
Published on Web 04/09/1999

covering the active site and its catalytic serine is solvent accessible (*10*). Furthermore, the oxyanion hole of the free enzyme is preformed in the protein crystal (*13*). This suggested that no significant rearrangements will occur upon binding of the substrate, which was subsequently confirmed by crystallographic studies of cutinase−inhibitor complexes (*13*, *17*). These findings were invoked to rationalize the phenomenon that cutinase lacks interfacial activation (*7*, *8*).

The dynamics of *F. solani pisi* cutinase has been studied through a structural comparison among different crystal forms of its variants (*18*) and by molecular dynamics (MD) simulations analyzed using the essential dynamics method, which allows identification of positions in the protein where concerted motions occur (*19*). These studies revealed some increased mobility in the substrate binding region. However, the internal mobility of cutinase or any other lipolytic enzyme has not been investigated by a direct experimental approach yet. As a first step in the study of cutinase by NMR spectroscopy, virtually complete assignments were made for the backbone and side chain ^{1}H, ^{13}C, and ^{15}N resonances (*20*). Furthermore, we presented an alternative approach for analyzing protein backbone ^{15}N relaxation data (*21*), which we will use in this report on the backbone dynamics of cutinase. We will relate the findings to its structure, mobility, function, and stability. In particular, we will assess whether the active conformation observed in the crystal structure of free cutinase is also preformed in solution, in relation to the absence of interfacial activation.

MATERIALS AND METHODS

Sample Preparation. Recombinant cutinase expression and purification procedures have been described previously (*20*). Lyophilized, uniformly ^{13}C- and ^{15}N-labeled cutinase was dissolved in buffer containing 10 mM deuterated sodium acetate (99.5% D), 100 mM NaCl, and 0.02% sodium azide (pH 5.0 unless stated otherwise). All buffers were filtered over sterile low protein-binding 0.22 μm filters. The H_2O samples were 95% H_2O/5% D_2O (99.9% D), and the D_2O sample was 100% D_2O (99.9% D). For the D_2O sample, the pH-meter readings were corrected for the isotope effect (*22*). The samples contained 2 mM cutinase, except for those prepared for measuring the temperature coefficients and pH titration shifts, which contained 0.2 mM cutinase.

NMR Spectroscopy. The measurement of ^{15}N relaxation has been described in Prompers et al. (*21*). For the R_1 measurements, spectra were recorded using relaxation periods of 4, 103, 203, 303, 403, 603, 803, 1003, 1403, 2003, and 3003 ms. For the R_2 experiments, spectra were recorded with relaxation periods of 4.29, 7.49, 8.58, 13.89, 14.98, 27.78, 41.66, 55.55, 69.44, 138.88, and 194.43 ms consisting of Carr−Purcell−Meiboom−Gill pulse trains. For the $R_{1\rho}$ experiments, spectra were recorded with relaxation periods of 8, 20, 40, 60, 80, 100, 120, 140, and 160 ms consisting of a CW spin lock with a frequency of about 2.7 kHz. For the NOE experiments, two spectra were recorded sequentially, one with and one without proton saturation. In the NOE experiment, a decoupling sequence was applied for 7 s to saturate the ^{1}H resonances. This was replaced by a prescan recovery delay of the same length in the reference spectrum. NOE and reference measurements were repeated three times.

Water-NOESY and water-ROESY experiments were carried out as modified versions of the enhanced PHOGSY (*23*). The pulse sequences are shown in Figure 1. NOEs or ROEs from $C^{\alpha}H$ protons resonating near the H_2O chemical shift were eliminated by a 90° ^{13}C purge pulse (*24*). The WATERGATE-HSQC of the original pulse sequence was replaced by the fast HSQC (*25*) to avoid water saturation. In the water-NOESY sequence, non-zero-order coherence present during τ_m was removed by a gradient pulse (G_2). During the remainder of τ_m, a weak gradient (G_3) was maintained to prevent radiation damping (*26*). A prescan recovery delay of 2 s was used. Water-NOESY spectra were recorded with mixing times of 50, 100, 200, and 400 ms at both 20 and 25 °C and water-ROESY spectra with 25, 50, and 200 ms spin-lock periods at 25 °C only.

Amide hydrogen exchange data were recorded starting with a freshly prepared D_2O sample at 25 °C and pH 5.0. Forty ^{1}H−^{15}N HSQC spectra were measured between 0.5 h and approximately 1 month after dissolving the lyophilized cutinase in D_2O. Amide proton temperature coefficients were determined from three ^{1}H−^{15}N HSQC spectra, recorded at 20, 30, and 40 °C, respectively. The pH titration shifts of the amide protons and nitrogens were characterized by measuring HSQC spectra of samples in a pH range between 4 and 10.

All experiments were performed on a Bruker 600 MHz AMX spectrometer equipped with a Bruker BLAX 300 W linear amplifier and a 5 mm inverse triple-resonance probehead (^{1}H/^{15}N/^{13}C) either with or without a self-shielded z-gradient coil. All experiments were carried out at 25 °C, unless stated otherwise. The spectral width in the ^{15}N dimension (ω_1) was 3102 Hz, and it was 7246 Hz in the ^{1}H acquisition dimension (ω_2). The amide hydrogen exchange and temperature coefficient data were collected with 128 complex points in t_1 and 1024 in t_2. The water-NOESY, water-ROESY, and pH titration spectra contain 256 complex points in t_1 and 1024 in t_2. The water-NOESY spectra were recorded with 64 scans, the water-ROESY spectra with 128 scans, the amide hydrogen exchange spectra with eight scans, and the spectra for measuring the temperature coefficients and pH titration shifts with 48 scans. Quadrature detection in the indirectly detected dimension was accomplished using the States−TPPI acquisition method (*27*).

Data Analysis. Spectra were processed and analyzed on Silicon Graphics workstations, using the Triad software package (Tripos Inc.). Convolution filtering of the time domain data with a Gaussian function was applied to the acquisition dimension to suppress the water signal (*28*). All spectra were apodized in t_1 and t_2 using a squared-cosine-bell function, except for the acquisition dimension of the spectra used to measure the pH titration shifts which was processed using a 50°-shifted squared-sine-bell function. Mirror-image linear prediction (*29*) to 4 times the number of points that were acquired was applied to the ^{15}N dimension of the spectra which were used to measure the temperature coefficients (with subsequent zero filling) and pH titration shifts to obtain final spectrum sizes of 1K × 1K. The other spectra were zero-filled in the ^{15}N dimension (t_1) to achieve the final sizes of 1K × 1K. Assignments were taken from Prompers et al. (*20*).

Conformational exchange processes on a time scale slower than the frequency of the $R_{1\rho}$ spin-lock field (~2.7 kHz) were

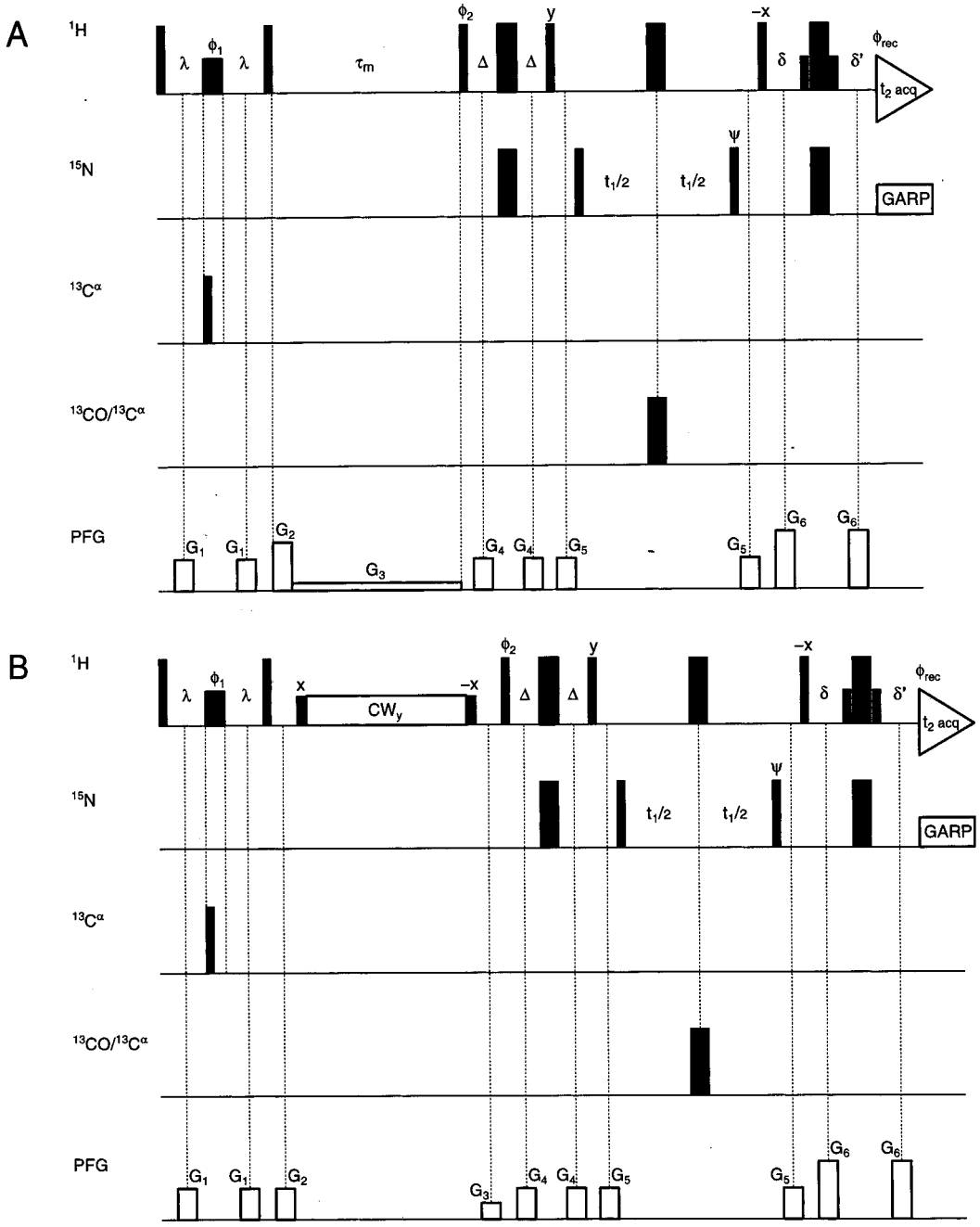

FIGURE 1: Pulse schemes for the (A) water-NOESY and (B) water-ROESY experiments. The narrow (wide) bars denote pulses with a flip angle of 90° (180°). H_2O-selective rectangular ^{1}H pulses are denoted by the smaller bars. Pulses for which the phase is not indicated are applied along the *x*-axis. The carbon pulses are generated using a single synthesizer, by jumping the frequency from 55 to 110 ppm after the mixing periods, and are applied with a 25 kHz field. Delay times are as follows: $\lambda = 3.57$ ms; $\Delta = 2.35$ ms; and $\delta = \Delta - p_{H_2O}$, where p_{H_2O} is the length of a H_2O-selective ^{1}H-90° pulse. The delay δ' was adjusted empirically starting from δ to refocus ^{1}H magnetization exactly at the first sampling point of the acquisition to give a 0° linear phase correction in the acquisition dimension. The spin lock in the water-ROESY experiment is achieved with a 2 kHz continuous pulse of phase *y*, flanked by an *x* and a $-x$ ^{1}H-90° pulse, applied at the same power. ^{15}N decoupling is achieved using a 1.25 kHz GARP sequence (*54*). The phase cycling was as follows: $\phi_1 = 2(x), 2(-y), 2(-x), 2(y)$; $\phi_2 = 2(x), 2(-x)$; $\psi = x, 2(-x), x$; and $\phi_{rec} = x, 2(-x), x$. Quadrature detection in t_1 was obtained by States−TPPI incrementation (*27*) of ψ. All gradients are sine-shaped and have durations of 100 μs, except for G_3 in the water-NOESY experiment, which is maintained during the entire mixing period. The following gradient strengths were used: $G_1 = 8$ G/cm, $G_4 = 13$ G/cm, $G_5 = 10.5$ G/cm, $G_6 = 50$ G/cm, and (A) $G_2 = 35.5$ G/cm and $G_3 = 0.1$ G/cm, and (B) $G_2 = 11.5$ G/cm and $G_3 = 4.5$ G/cm.

identified by calculating the difference between the ^{15}N R_2 and $R_{1\rho}$ relaxation rates (*30*) obtained from Prompers et al. (*21*).

Amide proton−deuterium exchange rate constants were derived from peak volumes. The rate constants were calculated by fitting a single-exponential decay function to the experimental data, using a three-parameter fit to the equation

$$I(t) = I_\infty + (I_0 - I_\infty) \exp(-k_{ex}t) \quad (1)$$

where $I(t)$ is the intensity at time t after addition of D_2O to the lyophilized protein, I_0 is the intensity at time zero, I_∞ is the intensity at $t = \infty$, and k_{ex} is the observed exchange rate

constant. The parameters were fitted using the SAS package (SAS Institute Inc.), applying the Levenburg−Marquardt algorithm (*31*, *32*). For amide protons that did not exchange completely before the last experiment was finished, and for which I_∞ was not well-determined, the decay curve was fitted using a final intensity of zero. Error estimates for the rates were obtained from the standard deviations of the curve fits. The intrinsic rate constants k_{rc} were obtained using the parameters from Bai et al. (*33*). Protection factors P were then calculated according to

$$P = k_{rc}/k_{ex} \quad (2)$$

Amide proton temperature coefficients were obtained by fitting a linear equation to the chemical shift versus temperature data (*34*).

RESULTS

Model-Free Analysis of ^{15}N Relaxation Data. The ^{15}N relaxation data were analyzed in terms of the model-free model (*35*−*38*) by directly fitting the model-free parameters to the peak volumes from which the relaxation rates and the NOE were derived (*21*). It was shown that cutinase could be approximated by an axially symmetric rotor, and anisotropy was included during the analysis. The results of the model-free analysis (*21*) are presented in Figure 2. Apart from the N-terminal propeptide,[2] the C-terminus, and two loop regions (residues 27−33 and 182−184), the backbone of cutinase appears to be mostly rigid on the picosecond to nanosecond time scale. Even though $R_{1\rho}$ data were used instead of R_2 data to minimize the effect of exchange contributions and even though anisotropy was included during the analysis, which would otherwise lead to misinterpreted exchange contributions (*21*), 42 residues still needed to be fitted with an exchange term. These residues are likely to experience different magnetic environments on a time scale faster than the frequency of the $R_{1\rho}$ spin-lock field (∼2.7 kHz), which we will refer to as the microsecond time scale in the remainder of this article. They are mainly located in loops, in the so-called flap helix of residues 81−85, and in one of the outer strands as well as at the N-terminal side of the β-sheet.

Comparison of R_2 and $R_{1\rho}$. Conformational exchange can provide an adiabatic relaxation pathway for transverse magnetization. The efficiency of relaxation of transverse magnetization locked along an effective magnetic field depends on the amplitude of the spin-lock field (*5*). The pulse train used during the ^{15}N T_2 relaxation delay has an effective spin-lock field strength of about 0.6 kHz, while the strength of the spin-lock field in the $R_{1\rho}$ experiment was about 2.7 kHz. Therefore, conformational exchange can be identified as an increased R_2 relaxation rate, compared to the $R_{1\rho}$ relaxation rate. Among the 184 residues for which both the ^{15}N R_2 and $R_{1\rho}$ relaxation rates could be determined, most residues have R_2 values that are higher than the $R_{1\rho}$ values (Figure 3). The rather systematic difference is probably due to the transient existence of nitrogen antiphase magnetization during the relaxation period of the R_2 experiments (*39*). This antiphase magnetization relaxes much faster than in-phase magnetization due to dipole−dipole interactions between the amide proton and other spatially close protons. For 28 residues, the difference between R_2 and $R_{1\rho}$ is even larger than 4 s^{-1} (Figure 3), while the standard deviation for the differences is on the order of 1.3 s^{-1}. These residues are likely to be involved in conformational exchange processes on a time scale slower than the frequency of the $R_{1\rho}$ spin-lock field (∼2.7 kHz), i.e., the millisecond time scale. Most of them are concentrated in three regions of the protein (Figure 4): (1) the loop of residues 40−52, which connects the strand of residues 34−39 and the helix of residues 53−63; (2) the loops (residues 73−80 and 86−91) connecting the flap helix of residues 81−85 to the core of the protein; and (3) the binding loop at the other side of the binding cleft (residues 171−191), containing active site residues Asp[175] and His[188]. These regions are all located in the binding site of the enzyme.

Analysis of Water-NOESY and Water-ROESY Spectra. In the water-ROESY spectra, the positive cross-peaks correspond to NHs which are in fast exchange with H_2O, while negative cross-peaks correspond to NHs in spatial proximity to bound H_2O or a rapidly exchanging hydroxyl proton. In the water-NOESY spectra, both types of cross-peaks are positive. Because $R_{1\rho}$ is much larger than R_1 for the amide protons, the water-ROESY spectra are inherently less sensitive than the water-NOESY spectra. For a number of residues, the water-ROESY signals were indeed below the level of detection, whereas their water-NOESY peaks could easily be observed. Whether the magnetization transfer was caused by exchange or by cross-relaxation could therefore not for all residues be determined from the sign of their water-ROESY signals. However, for most of the residues without observable water-ROESY peaks, the mechanism of magnetization transfer could be deduced from the ratio of the water-NOESY signal intensities at 20 and 25 °C. The intensity of cross-peaks due to fast exchange should decrease when the temperature is lowered, as the rates of exchange decrease approximately 3-fold with every 10 °C decrease in temperature (*40*). In contrast, cross-peaks due to cross-relaxation will be stronger or about equally intense, because τ_c increases when the temperature is lowered.

Only for eight residues could exchange peaks be observed. The low degree of occurrence of exchange peaks is in accordance with theoretical values for the intrinsic exchange rates (*33*) and the proton spin flip rate (estimated to be about 15 s^{-1} for the core of the protein) (*24*). For the highly mobile N-terminal and C-terminal residues, however, the exchange rate at which exchange peaks can be observed is lower than for the core residues; i.e., their exchange peaks can more readily be identified (*24*). Indeed, for the N-terminal residues Thr[3], Ser[4], and Asn[5], exchange peaks were observed. The other residues of the propeptide and the residues near the C-terminus do not have significant signals in the water-NOESY spectra, which is in accordance with their more restricted mobility compared to the tip of the propeptide (residues 3−5). The absence of an exchange peak for the C-terminal residue (residue 214) is probably caused by its extremely low intrinsic exchange rate (*33*). Contrary to expectation, also for five core residues exchange peaks were observed in the water-NOESY spectra. Gly[82] is positioned

[2] The 15 N-terminal residues constitute the propeptide of cutinase, not present in the mature enzyme. For convenience, we will refer to the 17 N-terminal residues as the propeptide in the remainder of this article.

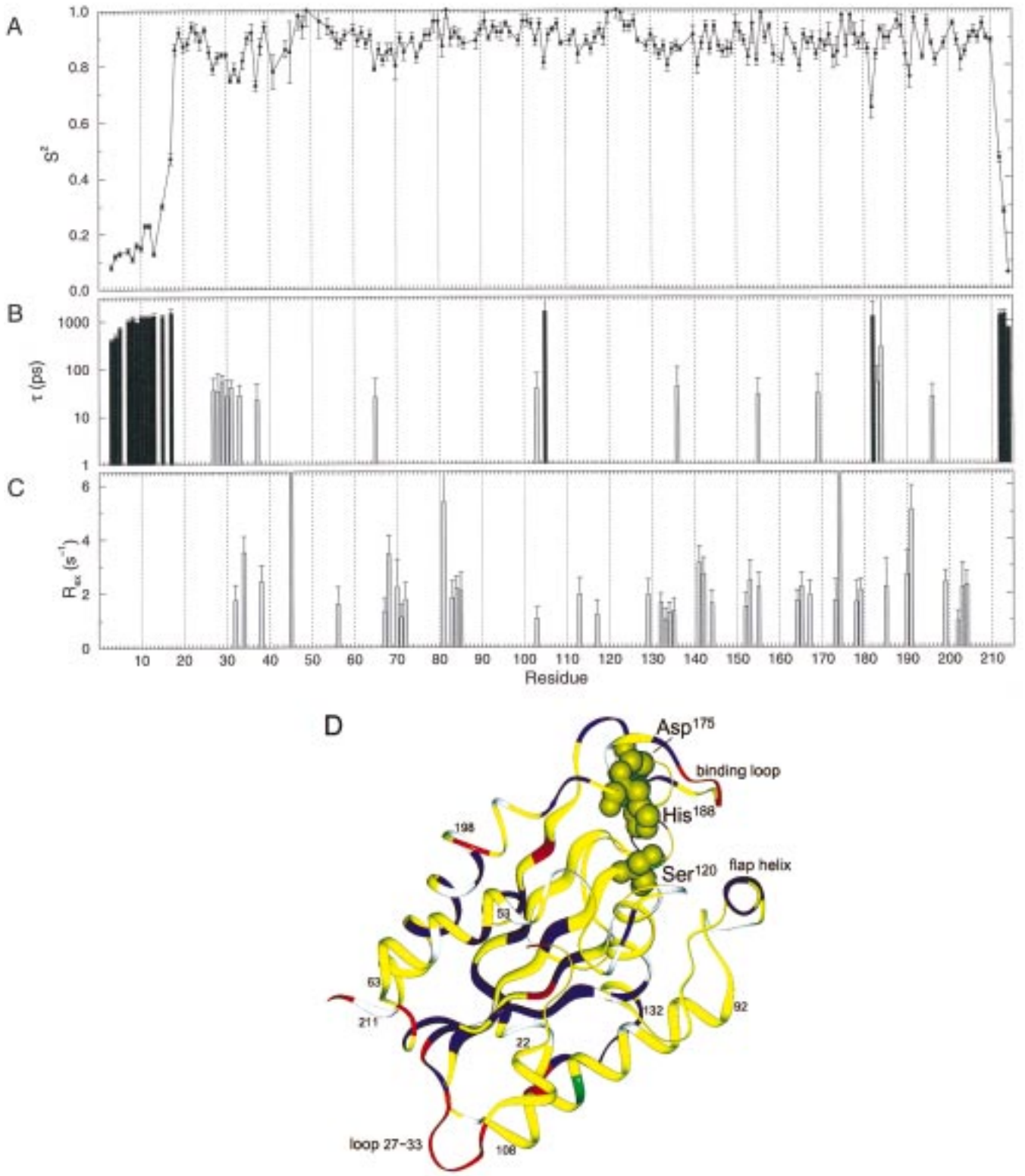

FIGURE 2: Model-free parameters for cutinase at an optimized τ_c of 10.80 ns using the axially symmetric anisotropic model (*21*): (A) generalized order parameter S^2, (B) internal correlation times τ_e (gray bars) and τ_s (black bars), (C) exchange contribution to $R_{1\rho}$ (the exchange contributions of residues 45 and 174 run off the scale, but were 11.86 ± 3.48 and 10.06 ± 1.91 s^{-1}, respectively), and (D) the model selection mapped on the crystal structure (*10*). In panel D, residues fitted without an internal correlation time or an exchange contribution are yellow, residues fitted with one or two internal correlation times are red, residues fitted with an exchange contribution to their $R_{1\rho}$ are blue, and residues fitted with an internal correlation time as well as an exchange contribution are green. Residues for which the model-free parameters could not be determined, i.e., prolines and residues with missing assignments or overlapping signals, are white. The β-strands are depicted by the broad ribbons, the helices by the intermediate ribbons, and the loops by the narrow ribbons, and the active site residues are shown in space filling representations. Residues 1−16 and 214 are missing from the ribbon, because they were not observed in the X-ray structure. Panel D was generated with the program Insight II (MSI).

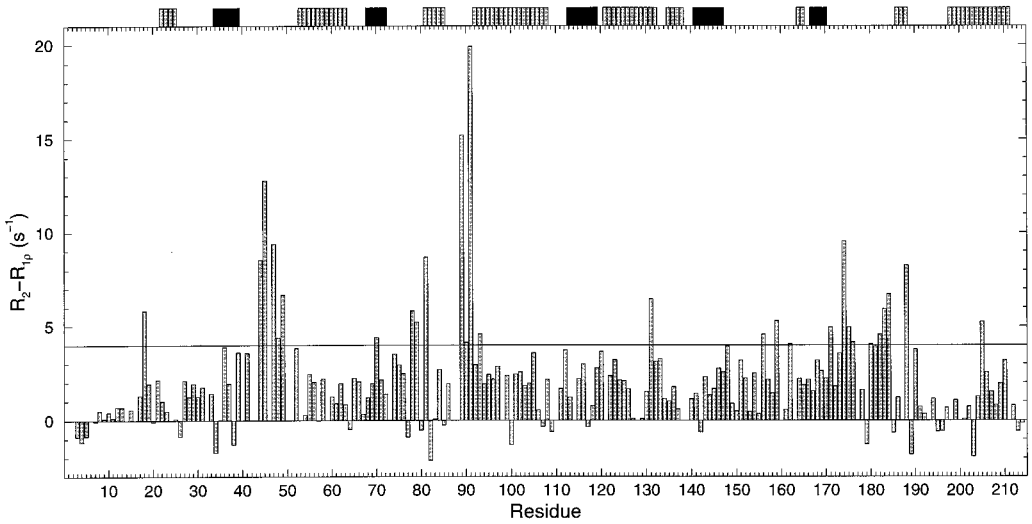

FIGURE 3: Differences between the ^{15}N R_2 and $R_{1\rho}$ relaxation rates obtained from Prompers et al. (*21*). A horizontal line is drawn at 4 s^{-1}. Residues in β-strands and helices are depicted by the black and gray bars, respectively, at the top of the figure.

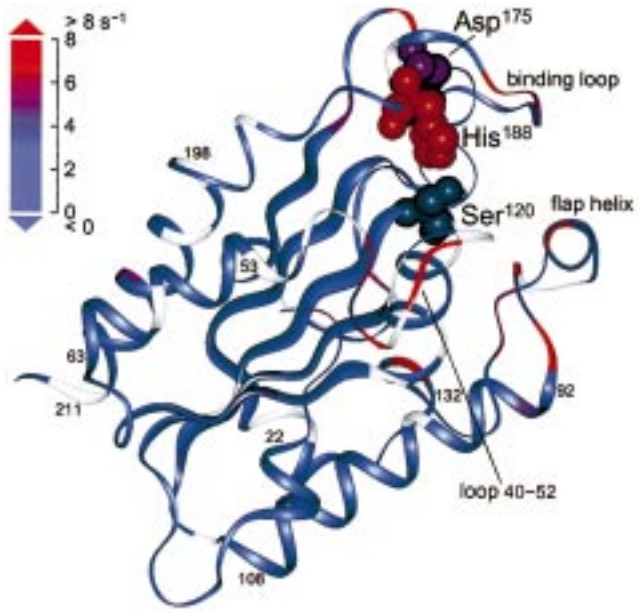

FIGURE 4: Differences between the ^{15}N R_2 and $R_{1\rho}$ relaxation rates obtained from Prompers et al. (*21*) mapped on the crystal structure (*10*). Residues for which the difference could not be determined, i.e., prolines and residues with missing assignments or overlapping signals, are white. The β-strands are depicted by the broad ribbons, the helices by the intermediate ribbons, and the loops by the narrow ribbons, and the active site residues are shown in space filling representations. Residues 1−16 and 214 are missing from the ribbon, because they were not observed in the X-ray structure. This figure was generated with the program Insight II (MSI).

at the N-terminus of the flap helix of residues 81−85, and Ser[92] and Ala[93] are positioned at the N-terminus of the helix of residues 92−108. These helices are both preceded by mobile loops (vide supra) connecting the flap helix to the core of the protein. Although conformational exchange does not need to contribute to amide hydrogen exchange, the millisecond time scale motions of these loops might accelerate the exchange of Gly[82], Ser[92], and Ala[93]. Their exchange could also be enhanced by the helix dipoles or, for Ser[92] and Ala[93], by the surrounding positively charged arginine residues. The exchange peaks observed for Thr[173] and Gly[174] may be explained by conformational exchange processes as well; Gly[174] has a very large exchange contribution to its $R_{1\rho}$ (10 ± 2 s^{-1}) (*21*). This implies that it adopts multiple conformations, which interconvert on a time scale faster than 2.7 kHz. No attempt was made to quantify the exchange rate constants for the residues with exchange peaks.

As a NOE/ROE to water cannot be distinguished from a NOE/ROE to a rapidly exchanging hydroxyl proton resonating at the H_2O chemical shift (*41*), the proximity to hydroxyl groups of serines, threonines, and tyrosines was checked for each amide proton in the crystal structure of cutinase (*10*). All side chains of aspartic and glutamic acids were assumed to be deprotonated at the pH of the sample used for the measurements as there was no evidence for any having pK_as in the range of 4−10 (vide infra). Among the residues exhibiting cross-relaxation signals in the water-NOESY spectra, 10 residues could be identified, of which the amide protons give an unambiguous NOE to bound water: Gly[41], Val[73], Asn[152], Leu[153], Gln[154], Ile[159], Leu[176], Val[177], Gly[180], and Ala[185]. These residues are all located around the binding site, which appears to be surrounded by bound waters, i.e., water molecules with a residence time of >300 ps. The NMR data can be fully explained using the five crystal waters in the X-ray structure (*10*) which have crystallographic *B*-factors comparable to the *B*-factors of atoms in the core of the protein (<16 Å^2) and which are not accessible to the solvent. In the crystal structure, there are five other crystal waters with low *B*-factors (<16 Å^2), but they are all solvent accessible, which apparently precludes their detection by NMR as they exchange with the bulk solvent too rapidly. Ordering the crystal waters by their solvent accessible surface shows that, besides the five crystal waters observed in solution, one other crystal water is inaccessible. However, this water molecule is less well defined (*B*-factor = 23.59 Å^2), suggesting mobility which will decrease the intensity of the NOE peaks to the amide protons of the protein (*42*). Another crystal water is only slightly accessible, but well-defined (*B*-factor < 16 Å^2). However, it is not close enough to any amide proton to give an NOE and can therefore not be detected.

Protection Factors and Temperature Coefficients. Amide hydrogen protection factors and temperature coefficients are plotted in Figure 5. All major secondary structural elements are protected from exchange, while the loop regions in

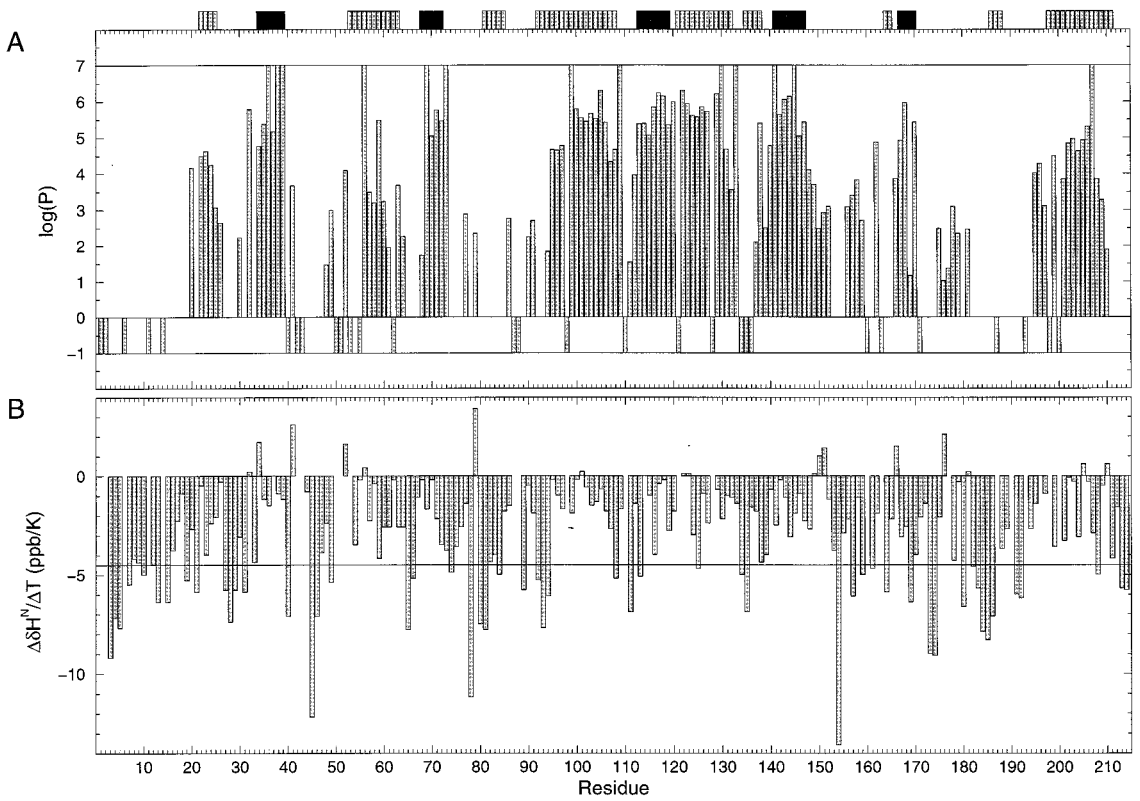

FIGURE 5: Amide hydrogen (A) protection factors and (B) temperature coefficients. A log(*P*) value of 0 was assigned to residues which exchanged too fast to be measured, and a log(*P*) value of 7 was assigned to residues which did not exchange to a significant extent after 1 month. Residues for which the protection factor could not be determined, i.e., prolines and residues with missing assignments or overlapping signals, were given a log(*P*) value of −1. Residues for which the temperature coefficient could not be determined due to the same reasons are omitted from the temperature coefficients graph. The horizontal line in this graph at −4.5 ppb/K denotes the value above which an amide is assumed to be hydrogen bonded and below which it is assumed not to be hydrogen bonded (*34*). Residues in β-strands and helices are depicted by the black and gray bars, respectively, at the top of the figure.

general exchange much faster. Most protected amide protons have temperature coefficients that are more positive than −4.5 ppb/K, which indicates that they are hydrogen bonded (*34*). On the other hand, most amide protons which exchange very fast have temperature coefficients that are more negative than −4.5 ppb/K, indicating that they are not hydrogen bonded. The amide protons which are subject to rapid exchange but with temperature coefficients that are more positive than −4.5 ppb/K are likely to be surface exposed but hydrogen bonded (*34*). The remaining protons which are protected from exchange but have temperature coefficients that are more negative than −4.5 ppb/K might be inaccessible but not hydrogen bonded. The protection factors and temperature coefficients are combined in Figure 6, which classifies the amides as hydrogen bonded, not hydrogen bonded, exposed but hydrogen bonded, or inaccessible but not hydrogen bonded as described above. From this figure, it can be seen that the amides in the latter two categories are mainly located in the two more mobile regions of the molecule, i.e., the binding site and the region at the N-terminal side of the β-sheet (Figures 2 and 4). Therefore, their temperature coefficients could also be affected by changes in the populations of substates, and their classification should be used with great care.

pH Titration. The amide signals of the following 12 residues shift moderately between pH 5 and 7: 80−82, 84, 85, 122, 172, 177, 188, 189, 194, and 205. Except for the latter two, all these residues are in the direct vicinity of the active site. Therefore, the observed shifts most likely reflect the titration of the active site His^{188}, which is the single histidine of cutinase and the only residue which is a priori expected to titrate in the pH range that was studied. From the pH titration profiles, an apparent pK_a of 5.8 can be deduced, which is close to the value of 6.5 estimated by Lauwereys et al. (*8*). Except for the pH titration, all other experiments described in this article were performed at pH 5.0, at which the active site His^{188} is protonated, whereas in the active enzyme it has to be deprotonated. This pH titration study shows that no major conformational changes occur due to the protonation or deprotonation of the active site His^{188}, which ensures that our results are functionally relevant. Asp^{194} is located before the C-terminal helix, and Glu^{205} is located in the middle of this helix, both quite distant from His^{188}. In addition to their own charged side chains, the amides of these residues are both surrounded by some other charged, exposed side chains. Their shifts during the pH titration are probably due to changes in the salt bridges at the exterior of the protein.

Backbone Dynamics of Cutinase. In the following, all available data are combined for each residue, which gives a very detailed picture of the backbone dynamics of cutinase on a time scale ranging from picoseconds to hours. The results are divided into five sections describing different parts of the protein's structure: the N-terminal propeptide, the central β-sheet, the helices covering the β-sheet, the turns and loops outside the binding region, and the binding site itself.

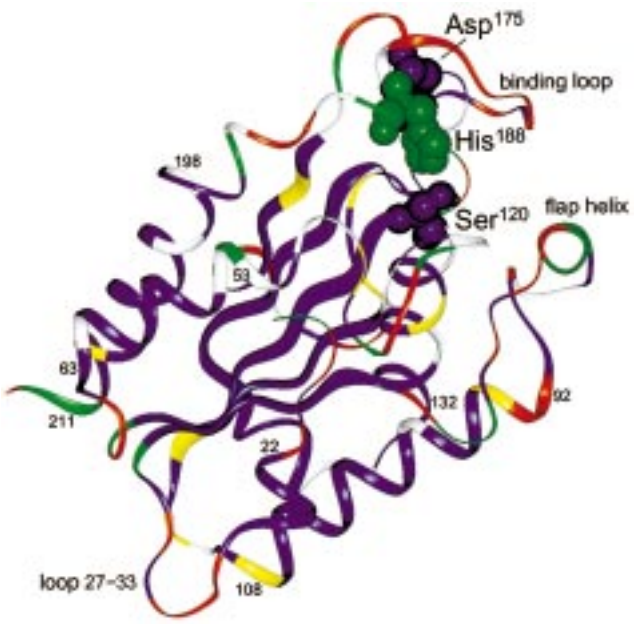

FIGURE 6: Amide hydrogen protection factors and temperature coefficients mapped on the crystal structure (*10*). Residues protected from D_2O exchange with temperature coefficients that are more positive than −4.5 ppb/K are purple, unprotected residues with temperature coefficients that are more negative than −4.5 ppb/K are red, unprotected residues with temperature coefficients that are more positive than −4.5 ppb/K are green, and protected residues with temperature coefficients that are more negative than −4.5 ppb/K are yellow. The purple residues are hydrogen bonded, the red residues are not hydrogen bonded, and the green residues are exposed but hydrogen bonded according to Baxter and Williamson (*34*). The yellow residues might be inaccessible but not hydrogen bonded. Residues for which the protection factor and/or temperature coefficient could not be determined, i.e., prolines and residues with missing assignments or overlapping signals, are white. The β-strands are depicted by the broad ribbons, the helices by the intermediate ribbons, and the loops by the narrow ribbons, and the active site residues are shown in space filling representations. Residues 1−16 and 214 are missing from the ribbon, because they were not observed in the X-ray structure. This figure was generated with the program Insight II (MSI).

N-Terminal Propeptide. The N-terminal propeptide is shown by the ^{15}N relaxation data to be very flexible on the picosecond to nanosecond time scale (Figure 2A,B). However, it does not seem to be completely unstructured. The main part of the propeptide (residues 7−17) has a rather uniform correlation time of about 1 ns for internal motions on the slower time scale of the extended model-free model (*37*, *38*). Residue 6 is a proline, a residue known for its ability to break secondary structural elements. The residues N-terminal to this proline (the tip of the propeptide) have faster internal mobility with internal correlation times ranging from 720 ps (for residue 5) to 400 ps (for residue 3). The order parameter gradually drops starting from the core of the protein, showing that the motions become increasingly less restricted toward the terminus. The 16 N-terminal residues were not observed in the crystal structure, whereas residue 17 has a very high *B*-factor (*10*), indicating that also in the protein crystal the propeptide is substantially more disordered than the remainder of the enzyme.

Central β-Sheet. The parallel β-sheet forms the central building block of the core of cutinase. It is constituted of five strands: residues 34−39, 68−72, 113−119, 141−147, and 167−170. All residues in the sheet, except residues 68 and 169 which will be described below, have very high protection factors ($>10^4$) and amide proton temperature coefficients that are more positive than −4.5 ppb/K (Figure 5), indicating that they are all hydrogen bonded (Figure 6). For some of them, no significant exchange could be detected even 1 month after dissolving the enzyme in D_2O, which is rather extreme. This indicates that the sheet must be a very stable structural element, even though it contains a bulge at residues 142 and 143 in the fourth strand and it is a parallel β-sheet, generally considered to be intrinsically less stable than an antiparallel β-sheet (*43*). In agreement with the exchange and temperature coefficient data, the sheet has hardly any internal mobility on the picosecond to nanosecond time scale according to the ^{15}N relaxation data (Figure 2). Figures 3 and 4 show that the sheet is rather rigid on the millisecond time scale as well. The rigidity of the β-sheet is also reflected in its side chains by the slow aromatic ring flips of Tyr^{38}, which is packed against the sheet and for which nondegenerate $^1H^{\delta}$ and $^1H^{\epsilon}$ signals were observed at 298 K (*44*). In accordance with our data, the five strands have the lowest *B*-factors of the whole protein in the crystal structure (*10*) and exhibit low mobility in MD simulations (*19*).

All the results so far provide us with a rather static picture of the β-sheet. However, the N-terminal residues of all five strands and residues 142 and 144 around the bulge, which is not packed against another strand and can be regarded as part of the N-terminal side of the sheet as well, needed an exchange contribution to their $R_{1\rho}$ in the model-free analysis (Figure 2). This might indicate some increased mobility on the microsecond time scale at the N-terminal side of the β-sheet, but could also be caused by the movement of nearby loops or slight reorientations of the covering helices. Residues 38, 70−72, and 117 also have an exchange contribution, but this is probably due to the millisecond mobility of the nearby loop of residues 40−52. Residues 68 and 169, each located in one of the two outer strands, are much less protected from D_2O exchange than the rest of the sheet (Figure 5A), probably due to the larger conformational variability at these sides or simply because of the lack of a hydrogen bonding partner.

Helices Covering the β-Sheet. The central sheet is covered by four α-helices: residues 53−63, 92−108, 121−132, and 198−211. They have contiguous stretches of residues with amide proton temperature coefficients that are more positive than −4.5 ppb/K and high, occasionally medium, protection factors (Figure 5). Therefore, these helices can be regarded as stable secondary structural elements (Figure 6). In the crystal structure (*10*), all four helices have low *B*-factors, but the *B*-factors tend to increase toward their C-termini, in accordance with the tendency of the protection factors to decrease toward the C-terminal ends. The helices are well-preserved in MD simulations (*19*), which is in agreement with their rigidity on the picosecond to nanosecond, microsecond (Figure 2), and millisecond (Figures 3 and 4) time scales according to the ^{15}N relaxation data, except for some residues described below.

The protection factors of the helix of residues 53−63 show the periodicity of an α-helix (Figure 5A). The residues which are packed against the core of the protein have high protection factors, whereas the residues which are more exposed have medium protection factors. However, all residues have temperature coefficients that are more positive

than −4.5 ppb/K (Figure 5B), indicating that they are all hydrogen bonded (Figure 6). Helix bending, stretching the side of the helix furthest from the sheet, could make the amides at this side more susceptible to exchange. The C-terminal end of the helix of residues 53−63 displays, besides its increasing *B*-factors (*10*), a large anisotropy in the 1.0 Å X-ray structure (*11*), corroborating the view that it undergoes bending motions. The conformational change of residues 64−66, C-terminal to the helix of residues 53−63, observed in MD simulations (*19*) might be related to the bending of this helix.

Although the helix of residues 92−108 is very stable, the amides of its first three residues exchange rapidly and have temperature coefficients that are more negative than −4.5 ppb/K (Figures 5 and 6), probably because they have no hydrogen bonding partner. For residues 92 and 93, exchange peaks could be observed in the water-NOESY spectra, implying that their exchange must be faster than their intrinsic exchange. Residue 93 undergoes conformational exchange on the millisecond time scale, as evident from the difference between its R_2 and $R_{1\rho}$ (Figures 3 and 4). The helix of residues 92−108 is preceded by a mobile loop, which connects the flap helix of residues 81−85 to the core of the protein and undergoes displacements also on the millisecond time scale. The motions of this loop could cause some fraying of the helix of residues 92−108 at its N-terminus, explaining the fast exchange and millisecond mobility observed there. However, the helix dipole and the surrounding charged residues might also play a role here.

Residue 131, at the C-terminal end of the helix of residues 121−132, appears to be mobile on the millisecond time scale as well (Figures 3 and 4). Residue 132 and the succeeding loop up to residue 135 have conformational exchange on a faster, microsecond time scale, as evident from their exchange terms in the model-free analysis (Figure 2). Still, residues 131 and 132 are moderately to highly protected from D_2O exchange and have amide proton temperature coefficients that are close to zero (Figures 5 and 6). Their low *B*-factors in the crystal structure (*10*) make helix fraying or bending at first sight less plausible. However, in MD simulations (*19*), residues 131 and 132 do have increased mobility. The difference between the crystallographic data and the simulations was explained by crystal contacts.

The difference between R_2 and $R_{1\rho}$ of residue 205, in the middle of the helix of residues 198−211, is indicative of millisecond mobility (Figures 3 and 4), while some residues N-terminal to residue 205 appeared to be mobile on the microsecond time scale (Figure 2). However, they are all protected from D_2O exchange and have amide proton temperature coefficients that are more positive than −4.5 ppb/K (Figures 5 and 6). The amide resonances of residue 205 shifted during the pH titration near pH 5.0, so local fluctuations not affecting the helix integrity possibly occur, like changes in the salt bridges at the exterior of the protein. For the C-terminal residues of the helix of residues 198−211, the protection factor gradually drops, leaving no significant protection for residue 211, likely caused by some fraying of the helix at its C-terminus. This fraying might be induced by the high mobility of C-terminal residues 212−214 on the picosecond to nanosecond time scale as is evident from the model-free analysis (Figure 2). The moderately high protection factors of residues 195−197, together with their amide proton temperature coefficients that are close to zero, indicate that they might form a transient, additional turn of the helix of residues 198−211. Residues 191−197 form an even longer N-terminal extension of the C-terminal helix in the X-ray structure (*10*), but there was no evidence for its existence in solution (*20*). In solution, this part might be less regular and less stable than the remainder of the helix, probably caused by the mobility of the preceding binding loop. This is corroborated by MD simulations (*19*), during which these additional turns unfold and refold several times. The difference between the crystallographic data on one hand and the NMR data and the simulations on the other can be explained by crystal contacts.

Turns and Loops Outside the Binding Region. In addition to the major secondary structural elements, two smaller helices outside the binding region of cutinase (residues 22−25 and 135−138) seem to be rather stable. The amides of residues 22−26 and 136−140 are moderately to highly protected from D_2O exchange and have consistently higher temperature coefficients (Figures 5 and 6). Accordingly, they appear to be rigid on the picosecond to nanosecond, microsecond (Figure 2), and millisecond (Figures 3 and 4) time scales according to the ^{15}N relaxation data. Residues 148−152 and 156−159 also have moderately high protection factors and temperature coefficients indicative of hydrogen bonding, and might form some transient structural elements as well. This is in agreement with the presence of a β-turn and a left-handed helical turn in the X-ray structure at these positions, respectively (*10*).

The majority of amides in loops outside the binding region which have not been described thus far (residues 18−21, 27−33, 64−67, 109−112, 153−155, and 160−166) are not protected from exchange and do not have temperature coefficients indicative of hydrogen bonding (Figures 5 and 6). Correspondingly, the loop regions generally have higher *B*-factors in the crystal structure (*10*) and higher mobility in MD simulations (*19*) than the sheet and the major helices. The ^{15}N relaxation data show that the loops, apart from low-amplitude vibrational and librational motions that are apparent from their order parameters which are <1, do not have any significant mobility on the picosecond to nanosecond time scale (Figure 2). Furthermore, they appear to be mostly rigid on the microsecond (Figure 2) and millisecond (Figures 3 and 4) time scales.

As an exception, residues 27−31, 33, and 65 show some increased flexibility on the picosecond to nanosecond time scale (Figure 2) with internal correlation times around 35 ps. The low-amplitude, high-frequency mobility observed for these residues agrees with the extremely high *B*-factors in the crystal structure (*10*) and the large positional fluctuations in MD simulations (*19*). The increased flexibility of the loop of residues 27−33 seems to be interrupted at Ala^{32}, which, in contrast to the preceding residues, is highly protected from exchange and has an amide proton temperature coefficient that is close to zero (Figures 5 and 6). This is due to an amide−aromatic hydrogen bond between Ala^{32} and the aromatic ring of Trp^{69} (*20*). The exchange contribution to the $R_{1\rho}$ of residues 32 and 67 (Figure 2) is most likely caused by small reorientations with respect to this aromatic ring.

Residues 152, 153, and 155 have an exchange contribution to their $R_{1\rho}$ (Figure 2), and residues 152−154 give rise to cross-peaks in the water-NOESY spectra which could

unambiguously be identified as NOEs to bound water. From the crystal structure (*10*), it could be deduced that they all bind to the same water molecule. The enhanced $R_{1\rho}$ relaxation rates of residues 152, 153, and 155 could be caused by slow exchange of this water molecule, i.e., on a time scale longer than its minimal residence time of 300 ps.

Binding Site. The binding site (residues 40−52, 73−91, 120, and 171−191) appears to be mostly rigid on the picosecond to nanosecond time scale according to the ^{15}N relaxation data (Figure 2), but it undergoes displacements on slower, microsecond and millisecond time scales as is evident from the exchange contributions to the $R_{1\rho}$ relaxation rates of 12 residues in the binding region in the model-free analysis (Figure 2) and the large exchange contributions to the R_2 relaxation rates of 20 residues compared to their $R_{1\rho}$ values (Figures 3 and 4), respectively. The amides of five residues in this region (42, 43, 50, 88, and 121) are apparently broadened to such an extent that they have never been detected in an HSQC spectrum (*20*). In agreement with the observed mobility, the amide protons of most residues in the binding site had exchanged with deuterons before the first spectrum was recorded after dissolving the protein in D_2O. The only contiguous stretch of protected residues with temperature coefficients that are more positive than −4.5 ppb/K is formed by residues 175−179 and 181 (Figures 5 and 6), suggesting that they form a helical turn like in the crystal structure (*10*).

The loop of residues 40−52 contains Ser^{42}, of which the main chain nitrogen and the O^{γ} together with the main chain nitrogen of Gln^{121} form the oxyanion hole. The amides of Ser^{42} and Gln^{121} are two of the resonances which have thus far not been identified (*20*), which indicates that the oxyanion hole is rather flexible in solution. This is in remarkable contrast to the crystal structure, in which it was found to be preformed (*13*). In solution, nearly the whole loop appears to be mobile on the millisecond time scale. The amides of residues 42, 43, and 50 are broadened beyond detection (*20*), and residues 44, 45, and 47−49 have a significantly larger R_2 compared to their $R_{1\rho}$ values (Figures 3 and 4). The amides of residues 46 and 51 seem to be broadened as well, but have overlap in the HSQC spectrum, and therefore, no reliable relaxation rates could be determined for these residues. The conformational exchange of Thr^{45} is still apparent in its $R_{1\rho}$ (exchange contribution = 12 ± 3 s^{-1}) (*21*), indicating that it moves on a somewhat faster time scale. The low crystallographic *B*-factors of this loop are probably due to crystal contacts, which is corroborated by MD simulations (*19*), showing large fluctuations for residues 42−45.

Residues 73−91 form one of the two binding loops of cutinase and contain the so-called flap helix of residues 81−85. The loops (residues 73−80 and 86−91) connecting the flap helix to the core of the protein are involved in conformational exchange processes on the millisecond time scale. Residues 78 and 79 in the loop N-terminal to the flap helix and residues 89−91 in the C-terminal loop have significant exchange contributions to their R_2 relaxation rates compared to their $R_{1\rho}$ values (Figures 3 and 4), while the amide of residue 88 in the C-terminal loop is broadened beyond detection (*20*). Except for residue 81, the flap helix itself does not have increased differences between R_2 and $R_{1\rho}$, implying that it moves as a whole on the millisecond time scale, opening and closing the binding site. Our results are corroborated by MD simulations (*19*), in which the flap helix displays an axial rotation, with residues 80 and 90 acting as hinge points. The reorientations of this helix probably lead to the exchange contributions needed for nearly all residues in the helix of residues 81−85 in the model-free analysis (Figure 2). The flap helix is not protected from exchange, but a number of residues in this helix have amide temperature coefficients that are more positive than −4.5 ppb/K (Figure 5), indicating that they might be surface exposed but hydrogen bonded (Figure 6). However, their temperature coefficients could also be affected by the mobility of the flap helix, inducing changes in the populations of substates. Residue 82 gives rise to exchange peaks in the water-NOESY spectra, implying that its exchange must be faster than its intrinsic exchange, which might be due to the mobility of the preceding loop or the helix dipole.

The backbone amide of the active site Ser^{120} does not experience any significant mobility on the microsecond (Figure 2) or millisecond (Figures 3 and 4) time scales. In contrast to most other residues in the binding site, it is highly protected from D_2O exchange and its temperature coefficient indicates that it is hydrogen bonded (Figures 5 and 6).

The second binding loop of residues 171−191 contains active site residues Asp^{175} and His^{188}. In this loop, seven residues (173, 174, 178, 179, 185, 190, and 191) have exchange contributions to their $R_{1\rho}$ in the model-free analysis (Figure 2) and nine residues (171, 174−176, 180, 182−184, and 188) have significant differences between their R_2 and $R_{1\rho}$ values (Figures 3 and 4), implying that it undergoes conformational rearrangements on approximately the same time scale as the other binding loop. The mobility of the loop of residues 171−191 is also apparent in MD simulations (*19*), where residues 179−187 move in conjunction with the flap helix and where residues 172−174 undergo a conformational change. Gly^{174} has a rather extreme exchange contribution to its $R_{1\rho}$ (10 ± 2 s^{-1}) (*21*), possibly due to similar changes in conformation. Together with residue 173, it gives rise to exchange peaks in the water-NOESY spectra, probably due to the same processes. Residues 182−184 are the only residues in the binding site displaying mobility on the picosecond to nanosecond time scale (Figure 2). These residues are located in the tip of the second binding loop, which is highly accessible and does not form any hydrogen bonds in the crystal structure and which, remarkably, is the only part of the binding region with increased *B*-factors (*10*).

In the loop of residues 40−52, residues 41, 51, and 52, which anchor this loop to the core of the protein, give rise to cross-relaxation signals in the water-NOESY spectra. For residue 41, the signal could unambiguously be identified as an NOE to a bound water molecule. For residues 51 and 52, the observed NOEs could be caused by contacts with the same water molecule (*10*), but they could also be due to an interaction with a nearby hydroxyl proton. In the first binding loop of residues 73−91, again, the residue which connects it to the scaffold of the enzyme, residue 73, makes contact with a bound water molecule. In the second binding loop of residues 171−191, residues 176, 177, 180, and 185 have NOEs to bound waters. From the X-ray structure (*10*), it could be deduced that residues 176, 177, and 185 bind to a single water molecule, while residue 180, together with

residues 152−154, makes interaction with another water molecule.

DISCUSSION

In this study, we report for the first time the detailed dynamical behavior of a lipolytic enzyme, *F. solani pisi* cutinase, in solution. The core of cutinase is constituted of a five-stranded parallel β-sheet covered by four α-helices. This part of the structure appears to be remarkably rigid on time scales ranging from picoseconds to hours. It forms a very stable scaffold on which the catalytic apparatus is built. The scaffold found in cutinase, named the α/β hydrolase fold (*12*), is shared by as many as nine families (*45*). These nine families exhibit little or no sequence similarity and comprise a broad area of unrelated proteins with different functions such as esterases, lipases, catalases, chemotactic proteins, and flavodoxins. The α/β hydrolase fold obviously provides a convenient general-purpose framework on which different catalytic machineries can be arranged without losing efficiency. The rigidity as found for the core of cutinase suggests that this is a general feature for the α/β hydrolase motif. Unfortunately, no extensive dynamical studies have been performed on any α/β hydrolase fold enzyme before. However, amide hydrogen exchange data on the chemotactic protein CheY (*46*) and flavodoxins (*47*) showed that also in these proteins the α/β core contains the stable nucleus.

When we examine the core of cutinase in somewhat more detail, it appears that the internal mobility at the C-termini of the β-strands is almost completely restricted, while the N-termini seem to allow somewhat more flexibility. The C-terminal side of the sheet apparently has to form a stable platform for the catalytic machinery. For the N-terminal side of the β-sheet, stability might be less important. This is also reflected in the data for the four major α-helices, which tend to be more mobile toward their C-termini, covering the N-terminal side of the sheet. The N-termini of the strands and the C-termini of the helices are connected by loops, which in general have increased mobility.

Of particular interest is the increased flexibility of the loop of residues 27−33, which seems to be anchored to the core of the protein by Ala^{32}. This is probably due to the amide−aromatic hydrogen bond between Ala^{32} and the aromatic ring of Trp^{69} (*20*), which might therefore be structurally important. Ala^{32} is positioned just before the β-strand of residues 34−39, and Trp^{69} lies in the strand of residues 68−72. The amide−aromatic hydrogen bond between these residues might stabilize the N-terminal side of the β-sheet by holding these two strands together. The alignment of the sequence of *F. solani pisi* cutinase with seven other cutinases (*48*−*50*) shows that *F. solani pisi* cutinase is the only cutinase so far with this type of amide−aromatic interaction. In six other cutinases, the Trp at position 69 is conserved, but a Pro rather than an Ala is found at position 32. We can only postulate that in these cutinases the stabilization is achieved by stacking of this Pro onto the Trp aromatic ring, as for none of these cutinases is a three-dimensional structure available. Noteworthy is the fact that cutinase from *Aspergillus orizae* (*50*), the only cutinase so far that lacks the Trp at position 69, has an additional disulfide bond compared to the other cutinases, connecting the helix of residues 53−63 and the strand of residues 68−72. It might well be that this disulfide bond is an alternative stabilization of the N-terminal side of the β-sheet.

Another very flexible part of cutinase is the propeptide, not present in the mature enzyme. An alternative way of interpreting the relaxation data of the tip of the propeptide compared to the description in the Results would be to extend the extended model-free model even further with another, third internal correlation time. The physical model behind it holds that the whole propeptide has a uniform slow internal correlation time of about 1 ns and that the tip of the propeptide undergoes additional, faster internal motions ($\tau \sim 100$ ps, not shown). These uniform lower-frequency motions of the main part of the propeptide suggest that residues 7−17 might form some transient form of secondary structure, like an α-helix. The central hydrophobic core of signal sequences has been shown to have a strong preference for an α-helical conformation, which may be required for the function of these signal sequences (*51*). The helix is often flanked by a proline residue at its N-terminus and a glycine residue at its C-terminus (*51*), as is also the case for the more structured part of the propeptide of cutinase.

Our results show that while the core of cutinase is highly rigid, its binding site adopts multiple conformations which interconvert on the microsecond to millisecond time scale and that the oxyanion hole is rather flexible in solution as well. In the crystal structure (*10*), cutinase has a rather open conformation, in which the hydrophobic binding site is exposed. The observed mobility in solution most likely represents the interconversion between open and more closed conformations. The flap helix seems to move as a whole, thereby opening and closing the binding site, like in a true lipase (*14*−*16*). The opening and closing motions are on a time scale which corresponds with the kinetics of the hydrolysis reaction, i.e., the millisecond range (*8*). This suggests that these conformational rearrangements may form the rate-limiting step in catalysis. A number of residues around the binding site make interactions with bound water molecules. These bound water molecules could play a role during the binding of cutinase to a lipidic interface. During binding to an interface, these water molecules might be displaced, increasing the mobility around their former positions, which might be necessary for substrate binding.

In contrast to the rest of the binding site, the backbone of active site Ser^{120} is highly rigid. Ser^{120} by itself connects the strand of residues 113−119 and the helix of residues 121−132 in a highly constrained loop with unfavorable backbone dihedral angles (*10*). This "nucleophile elbow" is highly conserved among the α/β hydrolases (*12*). Apparently, cutinase needs its catalytic serine to be in a constrained, well-defined conformation for substrate binding. The other two active site residues, Asp^{175} and His^{188}, are located in the flexible second binding loop. In solution, this part of the catalytic triad is probably only fixed into its proper position upon binding of the substrate (*52*).

The flexible active site and oxyanion hole observed in solution are in contrast with the X-ray analysis results of Martinez et al. (*10*, *13*), namely, that in the protein crystal, cutinase has a well-defined active site and a preformed oxyanion hole. An investigation of the dynamics of cutinase through a structural comparison among different crystal forms of its variants already showed that the two binding loops probably are more mobile than had been suggested

previously (*18*). The atomic resolution of the 1.0 Å X-ray structure allowed the detection of an appreciable extent of flexibility in the active site of cutinase, pointing out a "breathing" movement in the substrate binding region (*11*). The crystal structure probably represents one of the multiple conformations present in solution, which fortuitously is the active conformation. This active conformation is possibly selected during the crystallization process due to packing interactions at the hydrophobic binding site. In solution, the oxyanion hole is probably only rigidly formed upon binding of the substrate. We are currently addressing this issue by studying the dynamics of cutinase in complex with a substrate-like inhibitor (*52*).

In contrast to most other lipases, cutinase does not show an enhancement of its activity in the presence of a lipid−water interface (*7*, *8*). From crystallographic studies, it was rationalized that cutinase lacks interfacial activation, because it does not need any rearrangements to bind its substrate (*13*, *17*). However, the solution studies presented here unambiguously show that cutinase, in the absence of an inhibitor, is not fixed into its active conformation and does undergo conformational rearrangements. As an alternative, we propose that cutinase lacks interfacial activation because its active conformation is not stabilized between two hydrolysis cycles, e.g., by a stabilizing interaction between the lid and the remainder of the protein, as was proposed for coypu pancreatic lipase (*53*). The open conformation of the lid in "classical" pancreatic lipases is stabilized by interactions with the core of the protein, the colipase, and the β5 loop (*16*). While the residues which are responsible for these interactions are totally conserved among the classical pancreatic lipases, they are almost all different in coypu pancreatic lipase. Therefore, it was suggested that this lipase displays no interfacial activation because the interactions stabilizing the open conformation of the lid domain cannot exist (*53*), which is probably also the case for cutinase.

ACKNOWLEDGMENT

We thank A. J. Fellinger, M. C. D. van der Burg-Koorevaar, J. E. M. van Nieuwenhoven, P. Ravestein, and A. J. van de Wijngaard for the production and purification of the uniformly ^{13}C- and ^{15}N-labeled sample of cutinase, S. de Jong for help with the SAS package, and M. R. Egmond, L. D. Creveld, and J. de Vlieg for stimulating discussions.

REFERENCES

1. Karplus, M., and McCammon, J. A. (1981) *CRC Crit. Rev. Biochem. 9*, 293−349.
2. Brooks, C. L., III, Karplus, M., and Pettitt, B. M. (1988) *Adv. Chem. Phys. 71*, 14−21.
3. Dobson, C. M. (1993) *Curr. Biol. 3*, 530−532.
4. Jardetzky, O., and Schmitt, T. H. (1996) *Chemtracts: Biochem. Mol. Biol. 6*, 1−17.
5. Palmer, A. G., III, Williams, J., and McDermott, A. (1996) *J. Phys. Chem. 100*, 13293−13310.
6. Kolattukudy, P. E. (1984) in *Lipases* (Borgström, B., and Brockman, H. L., Eds.) pp 471−504, Elsevier, Amsterdam.
7. de Geus, P., Lauwereys, M., and Matthyssens, G. (1990) World Patent WO 90/09446.
8. Lauwereys, M., de Geus, P., de Meutter, J., Stanssens, P., and Matthyssens, G. (1991) in *Lipases: Structure, Mechanism and Genetic Engineering* (Alberghina, L., Schmid, R. D., and Verger, R., Eds.) Vol. 16, pp 243−251, VCH, Weinheim, Germany.
9. Verger, R. (1997) *Trends Biotechnol. 15*, 32−38.
10. Martinez, C., de Geus, P., Lauwereys, M., Matthyssens, G., and Cambillau, C. (1992) *Nature 356*, 615−618.
11. Longhi, S., Czjzek, M., Lamzin, V., Nicolas, A., and Cambillau, C. (1997) *J. Mol. Biol. 268*, 779−799.
12. Ollis, D. L., Cheah, E., Cygler, M., Dijkstra, B., Frolow, F., Franken, S. M., Harel, M., Remington, S. J., Silman, I., Schrag, J., Sussman, J. L., Verschueren, K. H. G., and Goldman, A. (1992) *Protein Eng. 5*, 197−211.
13. Martinez, C., Nicolas, A., van Tilbeurgh, H., Egloff, M.-P., Cudrey, C., Verger, R., and Cambillau, C. (1994) *Biochemistry 33*, 83−89.
14. Brzozowski, A. M., Derewenda, U., Derewenda, Z. S., Dodson, G. G., Lawson, D. M., Turkenburg, J. P., Bjorkling, F., Huge-Jensen, B., Patkar, S. A., and Thim, L. (1991) *Nature 351*, 491−494.
15. Derewenda, U., Brzozowski, A. M., Lawson, D. M., and Derewenda, Z. S. (1992) *Biochemistry 31*, 1532−1541.
16. van Tilbeurgh, H., Egloff, M.-P., Martinez, C., Rugani, N., Verger, R., and Cambillau, C. (1993) *Nature 362*, 814−820.
17. Longhi, S., Mannesse, M., Verheij, H. M., de Haas, G. H., Egmond, M., Knoops-Mouthuy, E., and Cambillau, C. (1997) *Protein Sci. 6*, 275−286.
18. Longhi, S., Nicolas, A., Creveld, L., Egmond, M., Verrips, C. T., de Vlieg, J., Martinez, C., and Cambillau, C. (1996) *Proteins: Struct., Funct., Genet. 26*, 442−458.
19. Creveld, L. D., Amadei, A., van Schaik, R. C., Pepermans, H. A. M., de Vlieg, J., and Berendsen, H. J. C. (1998) *Proteins: Struct., Funct., Genet. 33*, 253−264.
20. Prompers, J. J., Groenewegen, A., van Schaik, R. C., Pepermans, H. A. M., and Hilbers, C. W. (1997) *Protein Sci. 6*, 2375−2384.
21. Prompers, J. J., Groenewegen, A., de Jong, S., Hilbers, C. W., and Pepermans, H. A. M. (1999) *J. Biomol. NMR* (submitted for publication).
22. Glasoe, P. K., and Long F. A. (1960) *J. Phys. Chem. 64*, 188−190.
23. Dalvit, C., and Hommel, U. (1995) *J. Magn. Reson., Ser. B 109*, 334−338.
24. Grzesiek, S., and Bax, A. (1993) *J. Biomol. NMR 3*, 627−638.
25. Mori, S., Abeygunawardana, C., Johnson, M. O., and van Zijl, P. C. M. (1995) *J. Magn. Reson., Ser. B 108*, 94−98.
26. Sklenář, V. (1995) *J. Magn. Reson., Ser. A 114*, 132−135.
27. Marion, D., Ikura, M., Tschudin, R., and Bax, A. (1989) *J. Magn. Reson. 85*, 393−399.
28. Marion, D., Ikura, M., and Bax, A. (1989) *J. Magn. Reson. 84*, 425−430.
29. Zhu, G., and Bax, A. (1990) *J. Magn. Reson. 90*, 405−410.
30. Tjandra, N., Kuboniwa, H., Ren, H., and Bax, A. (1995) *Eur. J. Biochem. 230*, 1014−1024.
31. Marquardt, D. W. (1963) *J. Soc. Ind. Appl. Math. 11*, 431−441.
32. Press, W. H., Flannery, B. P., Teukolsky, S. A., and Vetterling, W. T. (1986) *Numerical Recipes: The Art of Scientific Computing*, Cambridge University Press, Cambridge, U.K.
33. Bai, Y., Milne, J. S., Mayne, L., and Englander, S. W. (1993) *Proteins: Struct., Funct., Genet. 17*, 75−86.
34. Baxter, N. J., and Williamson, M. P. (1997) *J. Biomol. NMR 9*, 359−369.
35. Lipari, G., and Szabo, A. (1982) *J. Am. Chem. Soc. 104*, 4546−4559.
36. Lipari, G., and Szabo, A. (1982) *J. Am. Chem. Soc. 104*, 4559−4570.
37. Clore, G. M., Driscoll, P. C., Wingfield, P. T., and Gronenborn, A. M. (1990) *Biochemistry 29*, 7387−7401.
38. Clore, G. M., Szabo, A., Bax, A., Kay, L. E., Driscoll, P. C., and Gronenborn, A. M. (1990) *J. Am. Chem. Soc. 112*, 4989−4991.
39. Peng, J. W., Thanabal, V., and Wagner, G. (1991) *J. Magn. Reson. 94*, 82−100.
40. Scholtz, J. M., and Robertson, A. D. (1995) *Methods Mol. Biol. (Totowa, N.J.) 40*, 291−311.

41. Otting, G., and Wüthrich, K. (1989) *J. Am. Chem. Soc. 111*, 1871−1875.
42. Otting, G., Liepinsh, E., and Wüthrich, K. (1991) *Science 254*, 974−980.
43. Creighton, T. E. (1993) *Proteins: Structure and Molecular Properties*, p 186, W. H. Freeman and Company, New York.
44. Prompers, J. J., Groenewegen, A., Hilbers, C. W., and Pepermans, H. A. M. (1998) *J. Magn. Reson. 130*, 68−75.
45. Brenner, S. E., Chothia, C., and Hubbard, T. J. P. (1997) *Curr. Opin. Struct. Biol. 7*, 369−376.
46. Lacroix, E., Bruix, M., López-Hernández, E., Serrano, L., and Rico, M. (1997) *J. Mol. Biol. 271*, 472−487.
47. Steensma, E., and van Mierlo, C. P. M. (1998) *J. Mol. Biol. 282*, 653−666.
48. Ettinger, W. F., Thukral, S. K., and Kolattukudy, P. E. (1987) *Biochemistry 26*, 7883−7892.
49. Sweigard, J. A., Chumley, F. G., and Valent, B. (1992) *Mol. Gen. Genet. 232*, 174−182.
50. Ohnishi, K., Toida, J., Nakazawa, H., and Sekiguchi, J. (1995) *FEMS Microbiol. Lett. 126*, 145−150.
51. Bruch, M. D., McKnight, C. J., and Gierasch, L. M. (1989) *Biochemistry 28*, 8554−8561.
52. Prompers, J. J., van Noorloos, B., Mannesse, M. L. M., Groenewegen, A., Verheij, H. M., Egmond, M. R., Hilbers, C. W., and Pepermans, H. A. M. (1999) *Biochemistry* (in press).
53. Thirstrup, K., Verger, R., and Carrière, F. (1994) *Biochemistry 33*, 2748−2756.
54. Shaka, A. J., Barker, P. B., and Freeman, R. (1985) *J. Magn. Reson. 64*, 547−552.

BI9827215